Advanced Materials Technologies

ADVANCED MATERIALS TECHNOLOGIES
www.advmattechnol.com

RESEARCH ARTICLE OPEN ACCESS

Highly Anisotropic Quasi-Direct Organic Metal Halide Hybrids: A Platform for Polarization-Sensitive Optoelectronics

Rijan Karkee[1,2] | Rafael R. Del Grande[2] | Yeonjoo Lee[1] | Jinkyoung Yoo[1] | Azza Ben-Akacha[3] | Biwu Ma[3] | Michael T. Pettes[1] | David A. Strubbe[2]

[1]Center for Integrated Nanotechnologies (CINT), Materials Physics and Applications Division, Los Alamos National Laboratory, Los Alamos, New Mexico, USA | [2]Department of Physics, University of California, Merced, California, USA | [3]Department of Chemistry and Biochemistry, Florida State University, Tallahassee, Florida, USA

Correspondence: Rijan Karkee (rkarkee@lanl.gov) | Michael T. Pettes (pettesmt@lanl.gov) | David A. Strubbe (dstrubbe@ucmerced.edu)

Received: 22 November 2025 | **Revised:** 6 March 2026 | **Accepted:** 6 April 2026

Keywords: electron-phonon coupling | first-principles calculations | organic metal halide hybrids | perovskites | Raman spectroscopy

ABSTRACT

Low-dimensional organic–inorganic metal halide hybrids (OMHHs) exhibit remarkable optical properties and enhanced environmental stability. We investigate a 1D OMHH with formula $C_4N_2H_{14}PbBr_4$, consisting of Pb–Br chains separated by organic cations, which shows a large Stokes shift (0.83 eV) and broadband emission. Through first-principles calculations and polarized Raman spectroscopy, we characterize the material's vibrational properties and identify the specific phonon modes that drive exciton self-trapping. Our novel GW/Bethe-Salpeter equation force formalism reveals that low-frequency phonons (~100100 cm^{-1}, primarily involving Pb–Br motions) couple strongly with excitons, with a remarkably high Huang-Rhys factor of 137 ± 4, and gives a pathway for ultrafast structural analysis during the absorption process. This phonon-exciton coupling mechanism explains the material's broadband emission and provides a pathway for controlling optical properties through vibrations and for tuning vibrations through optical excitations. The material also exhibits highly anisotropic optical properties and electronic transport, with bands that are dispersive along the Pb–Br chains but nearly flat in perpendicular directions, resulting in direction-dependent electrical conductivity that is calculated to be an order of magnitude higher along the chain direction and consistent with measurements. These combined properties make this system an excellent platform for polarization-sensitive optoelectronic devices.

1 | Introduction

Lower dimensional perovskites [1–3], i.e., ABX_3-based organic–inorganic metal halide hybrids (OMHHs), have recently received significant attention due to (i) an increase in stability against heat, light and moisture [4], and (ii) strong quantum confinement giving rise to excitonic physics for optoelectronics applications [5, 6]. The detailed mechanism of the increase in stability is not well understood. One argument for stronger resistance against moisture is due to replacement of unstable small hydroscopic organic cations with bulkier hydrophobic organic cations which strain the surface B-X bonds and repel the water molecules from reactive sites [1, 7]. Another thought is that there is a stronger van der Waals interaction between bulkier organic molecules and the B-X sublattice leading to better stability than in 3D perovskites [8]. This better stability could be interesting for solar photovoltaic applications. Mixed composites of 3D/2D perovskites [9] and 3D/1D perovskites [10] have been reported with relatively higher

stability than 3D versions. Low-dimensional perovskites having larger bandgaps are therefore exciting absorber materials in a perovskite tandem solar cell, to not only absorb high-energy photons but also act as a shield against degradation. Moreover, recent studies have demonstrated that targeted structural and chemical design in hybrid halides can enable multi-level information-security luminescence, nonlinear optical switching via phase transitions, and giant optical anisotropy, underscoring the versatility of this materials family [11–13].

A unique feature of lower dimensional perovskites is broadband white light emission as a result of exciton self-trapping [5, 14]. The excitons are the bound state of electron and hole held together by electrostatic Coulomb force. The self-trapped excitons are a type of exciton that generates a lattice distortion and becomes self-trapped by the distortion it induced. Self-trapped excitons can be considered excited state defects, as they exist only upon excitation and the lattice distortion disappears following decay to the ground state. With large-amplitude structural distortion, the resulting luminescence is often broad and has a large Stokes shift. The exciton self-trapping due to exciton-phonon interaction depends on dimensionality of the system [15, 16]. So, further lowering the dimensionality to 1D leads to greater self-trapping, due to the replacement of ionic bonds with van der Waals interactions and stronger localization of excitations. This effect has been observed in broadband luminescence with large Stokes shifts [17]. This could lead to an efficient white light emitter from a single material and has already been observed experimentally [5]. This could be very impactful, as creating effectively a high-quality white light from a single source is a challenge. In commercial white-light sources, one or more light-emitting diodes, coated by one or more phosphors are combined to yield white light. This combined emitter system can become problematic due to unequal degradation rates of different emitters. A single material that emits white light is therefore desired.

An example is N, N′-dimethylethylenediammonium lead bromide ($C_4N_2H_{14}PbBr_4$, also abbreviated as $DMEDAPbBr_4$) [5]. Due to its strongly anisotropic structure, resembling a bundle of nanowires, there naturally exists anisotropy in the absorption and emission of light in this material. While absorption anisotropy is relatively weak, our previous work [18] and recent findings by others on a similar material [19] have shown a pronounced anisotropy in emission. This observation raises intriguing questions because one would typically expect the polarization dependence to be similar in both absorption and emission if the same structures and states were involved. However, the photoluminescence intensity is maximized for linear polarization parallel to the 1D chains, regardless of the linear polarization of the excitation. This effect has been attributed to fast recombination caused by nonradiative recombination via surface defects or by the crystal structure distortion near the surface [18]. This experimental finding also hints at fascinating photophysics, most likely related to the self-trapped excitons that dominate the emission from these materials [5, 20, 21].

In this work, we perform a comprehensive first-principles study of the prototypical 1D OMHH, aiming to elucidate its anisotropic charge transport and optical properties and to unravel the mechanism of exciton self-trapping. We first examine the crystallographic structure of this hybrid, characterize the vibrations, and validate our computed structure against experiments via polarized Raman spectroscopy. We then analyze the electronic band structure, revealing a quasi-direct bandgap and highly anisotropic band dispersion. Using Boltzmann transport calculations and conductivity measurements, we quantify the directional dependence of electrical conductivity, which is found to be strongly enhanced along the chain direction. Next, we investigate the excited-state lattice dynamics associated with photogenerated excitons. We employ a novel methodology based on the GW/Bethe–Salpeter equation (GW-BSE) formalism to compute excited-state forces on the atoms [22–24]. This approach explicitly includes excitonic effects, in contrast to previous methods like the ΔSCF approach that neglect excitonic binding [21]. By projecting the GW-BSE forces onto phonon normal modes, we identify which vibrational modes couple most strongly to the exciton and drive the self-trapping distortion. Finally, through analysis of temperature-dependent photoluminescence (PL) spectra, we extract quantitative exciton–phonon coupling parameters (Huang–Rhys factor and phonon energy) and compare them with our theoretical predictions. Our study provides a microscopic picture of how a self-trapped exciton begins to form in a 1D perovskite and how this phenomenon, together with the material's intrinsic anisotropy, can be leveraged for novel optoelectronic technologies.

2 | Methodology

We used plane-wave density-functional theory (DFT) and density-functional perturbation theory (DFPT) [25] calculations in the Quantum ESPRESSO code [26, 27]. We used the Perdew-Burke-Ernzerhof (PBE) [28] exchange-correlation functional for all calculations except for Raman intensities [29], for which we used the local density approximation (LDA) functional [30]. ONCV pseudopotentials [31] from PseudoDojo [32] were used. A wavefunction energy cutoff of 816 eV and a $3 \times 3 \times 3$ half-shifted k-grid were used for self-consistent field (SCF) calculations. Forces and stresses were relaxed below 10^{-4} Ry/bohr and 0.1 kbar, respectively. For BerkeleyGW [23] calculations, we found that 330 empty bands, a $4 \times 4 \times 4$ q-grid, and a 204 eV screened-Coulomb cutoff converged GW quasiparticle corrections near the gap to within 100 meV. Excitons are computed with the Bethe-Salpeter equation in BerkeleyGW using eight occupied states and 12 unoccupied states and a $6 \times 6 \times 6$ fine k-grid, and are plotted with 0.1 eV Gaussian broadening. For interpolation of the GW band structure, 330 bands and a $4 \times 4 \times 4$ k-grid were used in the coarse grid. To obtain electron–phonon coefficients from DFPT in Quantum ESPRESSO, a Gaussian smearing of 0.001 eV was used. The electrical conductivity was calculated using the post-processing tool BoltzTrap2 [33] that solves Onsager transport coefficients for extended systems in a linearized Boltzmann transport equation framework. The BoltzTrap computation used non-self-consistent calculations on a half-shifted $30 \times 30 \times 30$ k-point mesh, and additional k-points were generated for band interpolation using a multiplier of 50.

The Raman spectroscopic measurements were conducted at ambient conditions in reflection mode using 1.6 mW 532.3 nm continuous wave excitation (Oxxius LCX-532S-100, single longitudinal mode diode pumped solid state laser), in a Horiba LabRAM HR Evolution high resolution confocal Raman microscope fitted

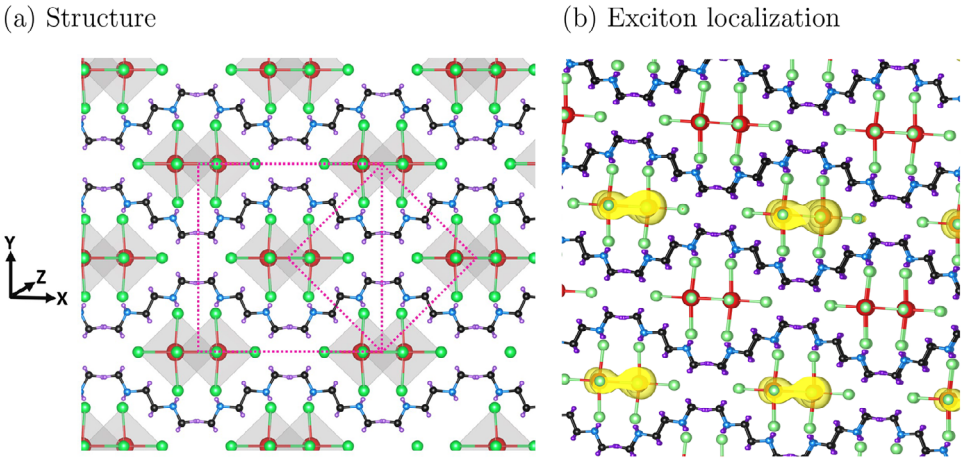

FIGURE 1 | (a) Structure of $DMEDAPbBr_4$ that has the Pb–Br chain into the page wrapped by the organic cations (red spheres: lead atoms; green spheres: bromine atoms; blue spheres: nitrogen atoms; black spheres: carbon atoms; purple spheres: hydrogen atoms; grey polyhedra: $PbBr_6^{4-}$ octahedra). Dotted square and diamond represent the conventional and primitive unit cells. (b) Localization of excitons on the Pb–Br chain, from GW/Bethe-Salpeter equation calculations. The isosurface shows the electron distribution given a hole location in a Br p orbital, which is the predominant nature of the valence band maximum.

with volume Bragg gratings. The experiment was configured using an 1800 mm^{-1} holographic grating blazed at 500, a 100 mm confocal hole diameter, and a 20×, 0.9 numerical aperture cover glass-corrected objective (Olympus LCPLFLN20XLCD, semi-apochromat). Spectral calibration was performed using the 1332.5 cm^{-1} band of a synthetic Type IIa diamond [34], and spectral intensity was calibrated using a VIS-halogen light source (NIST test no. 685/289682-17).

OMHH sample preparation follows methodology similar to that in Yuan et al. [5].

3 | Results

3.1 | Crystal Structure

The crystal structure of $DMEDAPbBr_4$ comprises a linear chain of Pb–Br atoms surrounded by organic molecules, making it a pseudo 1D material. This structure is classified under the *Imma* space group and exhibits D_{2h} point group symmetry. Through relaxation starting from the XRD structure [5] with initial lattice parameters (a = 14.62 Å, b = 6.10 Å, c = 14.40 Å, $\alpha = \beta = \gamma$= 90 = 90°), we obtained lattice parameters in close agreement (a = 14.70 Å, b = 6.06 Å, c = 14.56 Å, $\alpha = \beta = \gamma = 90°$). This level of agreement is consistent with our studies on other hybrid perovskites and OMHHs [35–37]. This structure has four formula units per cell. Our further calculations utilize a primitive cell of this body-centered structure with half the number of atoms, featuring lattice parameters $a = b = c$ = 10.80 Å, and angles $\alpha = 32.48°$, $\beta = 94.86°$, $\gamma = 85.88°$, with the Pb–Br chain oriented along the z direction. The structure, with the two definitions of unit cell, is shown in Figure 1. We also included the spin-orbit coupling (SOC) in the structural relaxation, and obtained essentially identical lattice parameters; for the primitive cell the relaxed lattice parameter is 10.801 Å without SOC and 10.803 Å with SOC (a difference of 0.002 Å).

3.2 | Raman Spectroscopy

We conducted both calculations and measurements of the polarized Raman spectra of this material, aiming to validate the consistency between experimental and theoretical results, and to characterize the vibrational properties. Our analysis revealed favorable agreement in the positions of most Raman peaks. To compensate for temperature effects, we multiplied the theoretical results by a factor of $\omega(1 - \exp\left(-\frac{\hbar\omega}{kT}\right))$ (where ω is the Raman shift and T= 300 K), which helps to compare to the calculated absolute Raman intensities as discussed in Strubbe et al. [38]. Remaining discrepancies in the relative intensities of these peaks and peak positions compared to the theoretical predictions may be due to limitations of the LDA intensity calculations (which more expensive hybrid functionals seem to improve [39]), inadequate treatment of the van der Waals interactions, anharmonicity, disorder [40], impurities or strain in the material. There are variations in the Raman activity of the modes depending on whether the polarization is parallel or perpendicular to the Pb–Br chain, which is due to the material's high anisotropy. In our previous work, it was shown by XRD that the needle-like crystals have the Pb–Br chain direction along their long axis [18]. The Raman peaks corresponding to directions parallel to the Pb–Br chain (parallel to z-direction) and other two directions have mostly B_{1g}, B_{3g}, and A_g symmetry (see Table S1), with the crystal's D_{2h} point group. From the peak-by-peak comparison in Table S1, the mean absolute deviation in Raman peak positions is 5.36 cm^{-1} (median 4.55 cm^{-1}; 12 out of /14 peaks within 10 cm^{-1}), and the near-zero mean signed deviation indicates no uniform systematic frequency shift.

Notably, the two perpendicular directions to the Pb–Br chain are not equivalent. By examining the polarized Raman results presented in Figure 2b, it becomes evident that considering the crystal's y-axis to be along the analyzer provides a closer match of the theoretical predictions to experiment than considering the x-axis to be along the analyzer. Polarized Raman spectroscopy

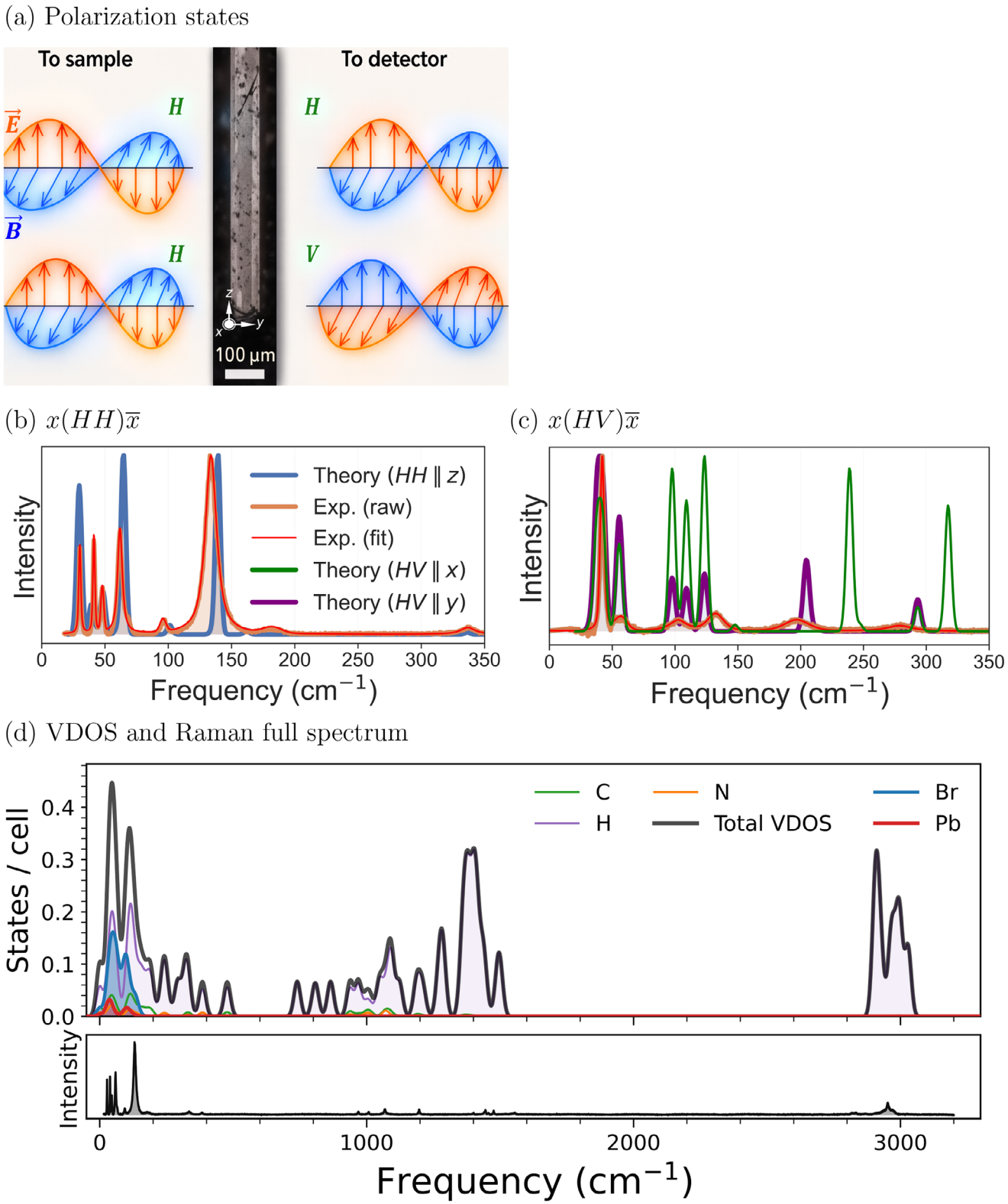

FIGURE 2 | Polarized Raman, vibrational density of states and Raman spectra from theory and experiment. (a) Polarization states used in the measurement (with polarizer and analyzer) and calculation, and a view of the 1D OMHH sample, where the Pb–Br chains are along the long needle axis [18]. (b) Raman spectrum with polarization parallel to Pb–Br chain ($H \| z-axis$, and (c) Raman spectrum with analyzer perpendicular to the chain (or $V \parallel y-$ axis). (b) and (c) share the same legend, calculated spectra for $H \| z-axis$ (blue line), $V \parallel x-$ axis (green line), and $V \| y-$ axis (purple line) are shown for comparison. (d) The vibrational density of states (VDOS), total and projected showing contributions of each atom type, compared to the experimental Raman spectrum (measured at room temperature), to show which atoms contribute to Raman activity in different frequency ranges.

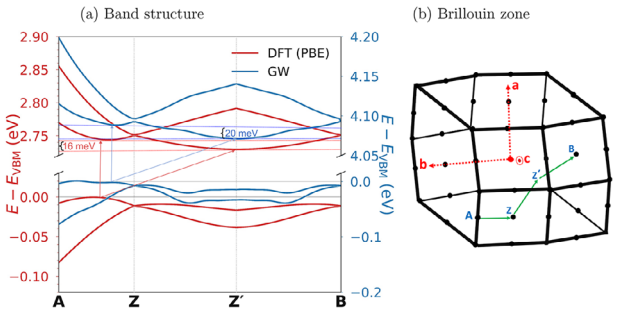

FIGURE 3 | (a) DFT and GW band structures of 1D perovskite, magnified to show band extrema and direct and indirect gaps. Band extrema are not at high-symmetry points. (b) k-point paths in Brillouin zone used for band structure. The k-points used in this plot are: A (−0.477 0.273 0.731), Z (0.249 0.249 −0.249), Z′ (−0.196 −0.190 0.294), and B (0.000 −0.500 −0.000), in reciprocal lattice units.

thus identifies the lattice orientation by comparison against theoretical calculations. In Figure 2a,b, we show the calculated and measured Raman spectra for $x(HH)\overline{x}$ and $x(HV)\overline{x}$, where $H \parallel z$ – crystallographic axis, and $V \parallel y$ – axis. Figure 2d shows the vibrational density of states (VDOS), which informs which atoms contribute to the vibrational modes. Clearly, we see the significance of Pb and Br atoms up to 300 cm^{-1}, and hence we are only focusing on that range for Raman, as higher-frequency modes mostly correspond to organic molecules. These findings highlight the importance of taking into account polarized Raman spectroscopy, especially in anisotropic materials. Surprisingly, this material has only weak anisotropy in dielectric tensor, which is diagonal in D_{2h}. The diagonal elements of the static electronic contributions to the dielectric tensor (ε_∞) are $\varepsilon_{xx} = 3.55$, $\varepsilon_{yy} = 3.56$, and $\varepsilon_{zz} = 3.64$. Evidently, this material's anisotropy of the Raman tensors [29] $A = \partial\varepsilon/\partial u$ is due to the vibrational anisotropy rather than dielectric anisotropy.

3.3 | Electronic Band Structure and Anisotropic Transport

We performed a detailed characterization of the electronic band structure at the DFT level. Unlike the typical scenario where band extrema occur at high-symmetry points, in this system, these extrema are slightly shifted away from such points. This deviation from high-symmetry points is reminiscent of what is observed in other spin-orbit semiconductors, such as Bi_2Te_3 [41–43]. Interestingly, even though this structure does have strong spin-orbit coupling due to the heavy Pb atoms and Br atoms within the compound, and has a calculated gap reduction of 0.5 eV due to spin-orbit [18], we find these deviations of the extrema even for our calculations here without spin-orbit coupling. We systematically explored the Brillouin zone to identify the band extrema, which allowed us to determine both the direct and indirect bandgaps, as illustrated in Figure 3. Notably, we find that the lowest energy transition is an indirect bandgap, but the material is essentially "quasi-direct-gap": the direct gap at the Brillouin zone center is only slightly (16 meV, on the order of kT) higher in energy than the indirect gap. We use the term quasi-direct to denote a band structure in which the indirect gap lies only slightly below the direct gap, with an energy separation comparable to (or smaller than) the thermal energy scale k_BT at operating temperature. This usage is consistent with recent literature employing "quasi-direct" to describe systems with very small direct–indirect separations [44–46]. We anticipate that the emission properties of this material will essentially resemble those of a direct-gap semiconductor, particularly at room temperature and above. The understanding of these quasi-direct features in the electronic structure is important for predicting the material's optical properties and its behavior under various conditions, and has been an interest for other optoelectronic applications [47]. Also note that a similar result as above is obtained with inclusion of self-energy in the GW approximation, leading to a gap increase of 1.30 eV [18]. The direct-indirect gap difference from GW is 20 meV. The near-degeneracy of direct and indirect gaps is an interesting feature, as it implies that the material can potentially absorb and emit photons efficiently (unlike typical indirect-gap semiconductors) while still having some characteristics of an indirect gap that might affect carrier dynamics at low temperature (for example, slightly slower radiative recombination or a temperature-dependence due to phonon assistance for the lowest-energy transition).

A striking aspect of the band structure is its high anisotropy. Bands dispersing along the chain direction (Γ–Z direction in the Brillouin zone) are steep and highly dispersive, indicative of small effective masses for electrons and holes along the Pb–Br chain. In contrast, dispersion along directions perpendicular to the chains (e.g., Γ–X or Γ–Y) is almost flat for the band-edge states, implying very large effective masses (electrons/holes are nearly immobile in those directions). This is consistent with the 1D nature of the inorganic network: carriers can move freely along the continuous chains but are confined by insulating organic barriers in the perpendicular directions. To quantify this, we calculated the direction-dependent electrical conductivity σ using Boltzmann transport theory. The tensor is diagonal due to D_{2h} symmetry. Our calculations reveal significant anisotropy. Notably, at the band edges, electrical conduction primarily occurs along the Pb–Br chain direction (σ_{zz}). This means charge transport is highly 1D in this material – it behaves like a bundle of nanowires electrically. Such pronounced transport anisotropy has clear implications for device design: any electrical device employing this material (e.g., a transistor or photodetector) would need to be oriented or textured such that the Pb–Br chains are aligned with the desired current flow direction to achieve optimal performance. For instance, a film or array of these 1D crystals could be aligned so that the chain axis is parallel to the electrodes to maximize conductivity. This finding suggests that, for device applications, the optimal voltage bias direction should align with the Pb–Br chain. In Figure 4, we can observe the band structure and electrical conductivity along both the parallel (z) and perpendicular (x and y) directions with respect to the Pb–Br chain. The curvature of the band structure is closely related to the electrical conductivity, with stronger curvature indicating higher electrical conductivity. Figure 4a,b exhibit consistent behavior. They highlight the substantial anisotropy in electrical conductivity, both parallel and perpendicular to the Pb–Br chains. Furthermore, there are noticeable differences in electrical conductivity between the two perpendicular directions. These distinctive properties, coupled with the anisotropy of optical absorption that we've previously observed, suggest the potential utility of this material in direct-polarization detector devices [48]. Such devices could

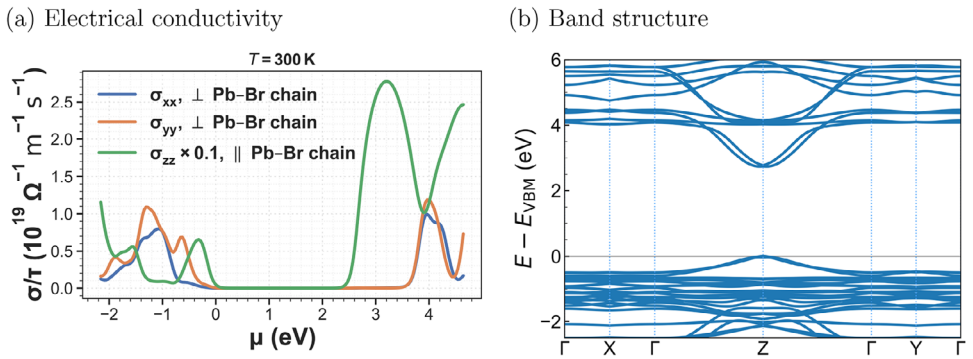

FIGURE 4 | (a) Electrical conductivity along different directions. The much larger σ_{zz} has been reduced by a factor of ten for easier comparison of curves. x and y are perpendicular directions to the Pb–Br chains, and z is parallel to the Pb–Br chains. (b) Band structure. Since we used the primitive unit cell, the k-point paths in Brillouin zone used for band structure are: X (0.251 0.251 0.251), Y (0.250 −0.250 −0.250), and Z (0.249 0.249 −0.249), which are obtained by converting X (0.5 0.0 0.0), Y (0.0 0.5 0.0), and Z (0.0 0.0 0.5) from conventional unit cell to the primitive cell.

take advantage of the material's anisotropic electrical and optical properties, offering new possibilities for practical applications.

To complement the calculated conductivity tensor, we performed direction-dependent DC I–V measurements on individual needle-like single crystals, where the needle axis corresponds to the Pb–Br chain direction [18]. Because the crystals are extremely resistive, an initial four-probe configuration did not yield a measurable inner-probe voltage drop, indicating that the sample resistance exceeded the practical sensitivity of that setup. We therefore estimated the resistivity along the needle axis using a two-probe approach with Pt-wire contacts fixed by Ag epoxy and optical-microscopy (OM) determination of the contacted segment geometry (see Figures S4 and S5). Assuming comparable contact resistance between measurements, this procedure gives an estimated axial resistivity of $\rho_{\parallel} \approx 8.6 \times 10^{9}\ \Omega \cdot \mathrm{cm}$. To probe transverse transport, we fabricated patterned electrodes on glass and bridged them with a perovskite rod; no measurable current was detected up to 20 V with 1 fA source measure unit (SMU)S. resolution, implying $R_{\perp} > 2 \times 10^{16}\ \Omega$ (conductance below the measurement floor). These measurements support strongly anisotropic, effectively 1D charge transport, while also highlighting key experimental challenges for fully quantitative tensor extraction, including extremely high resistances and contact-resistance uncertainty in two-probe geometries.

Despite the strong anisotropy in electrical conductivity, the Seebeck coefficient (Figure S2) shows only weak anisotropy, with $S_{xx} \approx S_{yy} \approx S_{zz}$ over most chemical potentials. This decoupling is useful for thermoelectric optimization because the power factor $S^2\sigma$ can then be maximized by orienting devices along the high-conductivity axis without significantly reducing S, as observed in other anisotropic thermoelectrics where S remains nearly orientation-independent [49].

Interestingly, the anisotropy is evident not only in charge transport but also (to a lesser degree) in optical absorption and emission. From our calculations and prior experiments [18], light polarized parallel to the chains is absorbed slightly more strongly than light polarized perpendicular to the chains. The difference in absorption is moderate (since even perpendicular polarization can still excite across the bandgap, albeit involving different electronic transitions), but the difference in emission polarization is much more pronounced. Because exciton self-trapping localizes the emitting state on a single chain, the emitted photons tend to be polarized along that chain's axis, regardless of how the exciton was initially created. The combination of anisotropic conductivity and polarized optical response suggests that this OMHH could serve as the functional material in polarization-sensitive optoelectronic devices. In particular, one can envision a polarized photodetector or polarization-resolved sensor where this material is used as the active medium: such a device would preferentially conduct or generate photocurrent for one light polarization over the orthogonal polarization. Our results indeed indicate that the material's unique anisotropy, in both its electrical and optical characteristics, can be harnessed to design novel detectors that directly encode polarization information without the need for external polarizing elements.

3.4 | Exciton-Phonon Coupling

When a system absorbs a photon, it goes from the ground state to an excited state and in doing so, it goes to a new potential energy surface, which is different from the ground state potential energy. Therefore, the ions experience forces toward the new minimum, which are the excited-state forces, and are involved in phenomena such as DNA degradation after absorption of UV light [50], self-trapped excitons [20, 51] and the stability in solar cell materials [52, 53].

We calculate excited-state forces as $F_{\mathrm{total}} = F_{\mathrm{DFT}} + F_{\mathrm{EX}}$, where F_{DFT} is the ground-state DFT force and F_{EX} is the force due to excitation [22]. The excited-state forces can be projected from an atomic/Cartesian basis to a ($q = 0$) phonon basis. This conversion reveals the contributions of significant phonon modes. In our specific case, we have identified vibration modes 23 (57.44 cm^{-1}, A_g) and 27 (99.98 cm^{-1}, B_{1u}) as the most influential, as shown in Figure 5. To quantify their dominance, we normalized the mode-resolved force projections: mode 23 (A_g) contributes 47.5% and mode 27 (B_{1u}) contributes 52.5% of the combined weight of these two modes. The low-frequency vibration modes are mostly due to Pb and Br atoms as shown in vibrational density of states, Figure 2d. The displacements due to the excited-state forces are in the direction of expansion and contraction of Pb–Br octahedra, which is consistent with the constrained DFT

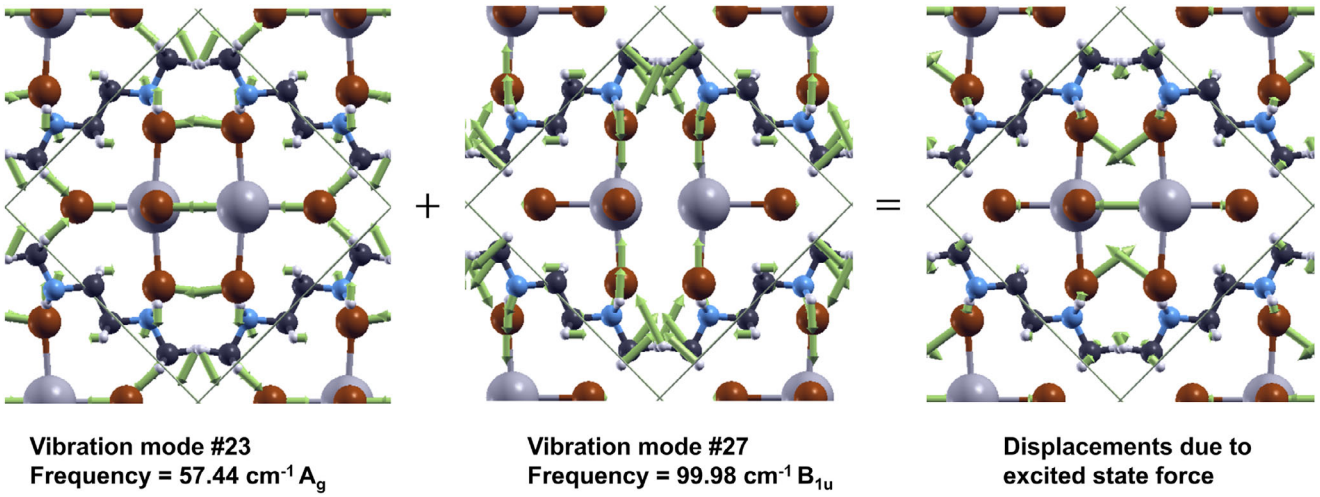

FIGURE 5 | Excited-state forces in the lowest exciton, shown by green arrows, and resolved into the contributions of the two most significant vibration modes.

results of Jiang et al. [21], although our primitive cell calculations cannot capture the long-range deformations studied in that work. Our GW/BSE excited-state force analysis provides insights into the coupling between excitons and phonons, indicating their interplay in the lattice deformation during excitation of light.

We plot the exciton–phonon coupling in Figure 6 for the lowest six excitons. Most excitons couple with a phonon of frequency 99.98 cm^{-1}, which is equivalent to 12.39 meV. For comparison, we extracted the temperature-dependent PL from Yuan et al. [5] and fitted the peaks to a Gaussian to determine the full-width at half-maximum (FWHM). We fitted the temperature dependence of this data using Equation (1), as has been done in other literature for an inorganic double perovskite with self-trapped excitons [54]:

$$FWHM = 2.36\sqrt{S}\hbar\omega_{\text{phonon}}\sqrt{\coth\frac{\hbar\omega_{\text{phonon}}}{2k_BT}} \quad (1)$$

This equation is appropriate for defect-related absorption, in which the structural change after absorption is dominated by one main phonon of frequency ω_{phonon}. [55–57] This fitting process has yielded two crucial parameters: the Huang-Rhys factor (S), which reflects the strength of the coupling between electrons and phonons, and the phonon frequency ω_{phonon}. [58] The fitted graph is presented in Figure 7, revealing a substantial Huang-Rhys factor of 137 ± 4. The Huang-Rhys factor S provides a compact measure of exciton–phonon coupling strength and corresponds approximately to the average number of phonons involved in the lattice relaxation accompanying an optical transition (larger S indicates stronger coupling). Reported Huang-Rhys factors in low-dimensional hybrid metal halides span from $S < 3$ in narrow-band 2D Ruddlesden–Popper perovskites to $S \sim 50$–180 in self-trapped-exciton emitters; the large value extracted here ($S = 137 \pm 4$) places $C_4N_2H_{14}PbBr_4$ near the upper end of the strong exciton–phonon-coupling regime (Table S2). This shows the strong exciton-phonon coupling in our system. The associated phonon energy is approximately 11 ± 1 meV, which aligns well with the simulated phonon frequency of 99.98 $cm^{-1} \approx 12$ meV.

The current calculation based on a primitive unit cell may not incorporate localized displacements due to excitons because of the translation symmetry of the crystal. Previously shown calculations using constrained DFT indicated that self-trapped excitons can localize in specific regions of the Pb–Br chain [21]. This implies that a larger supercell is the appropriate setting to break translational symmetry and capture a truly localized electron–hole pair and its accompanying distortion. Even within this constraint, our primitive-cell GW–BSE force calculation already recovers the most important local physics of self-trapping: (i) it identifies the phonon manifold most strongly coupled to the photoexcited state, (ii) predicts the displacement pattern, and (iii) yields a dominant coupling frequency near 100 cm^{-1} when the exciton forces are projected onto the phonon eigenmodes. Crucially, this predicted coupling scale quantitatively matches the phonon energy extracted from the temperature dependence of the PL linewidth. This experiment–theory consistency shows that, despite the absence of explicit real-space localization in the primitive cell, the GW–BSE force method correctly pinpoints both the active normal mode(s) and the effective coupling strength that drive STE formation, thereby providing a validated benchmark and a reliable starting point for forthcoming supercell studies that will capture full exciton localization and configuration-coordinate energetics. In that next step, the displacement field recovered here can be used as a physically informed initial distortion in a supercell relaxation to obtain the fully localized STE structure and its emission energetics.

4 | Outlook – Technological Potential

The unique combination of properties found in this 1D hybrid perovskite – namely, its highly anisotropic optical/electrical behavior and its ability to sustain self-trapped excitons with broadband emission – makes it a compelling material for innovative photonic technologies. One immediate possibility is in polarization-sensitive photodetectors. Because the material's conductivity and

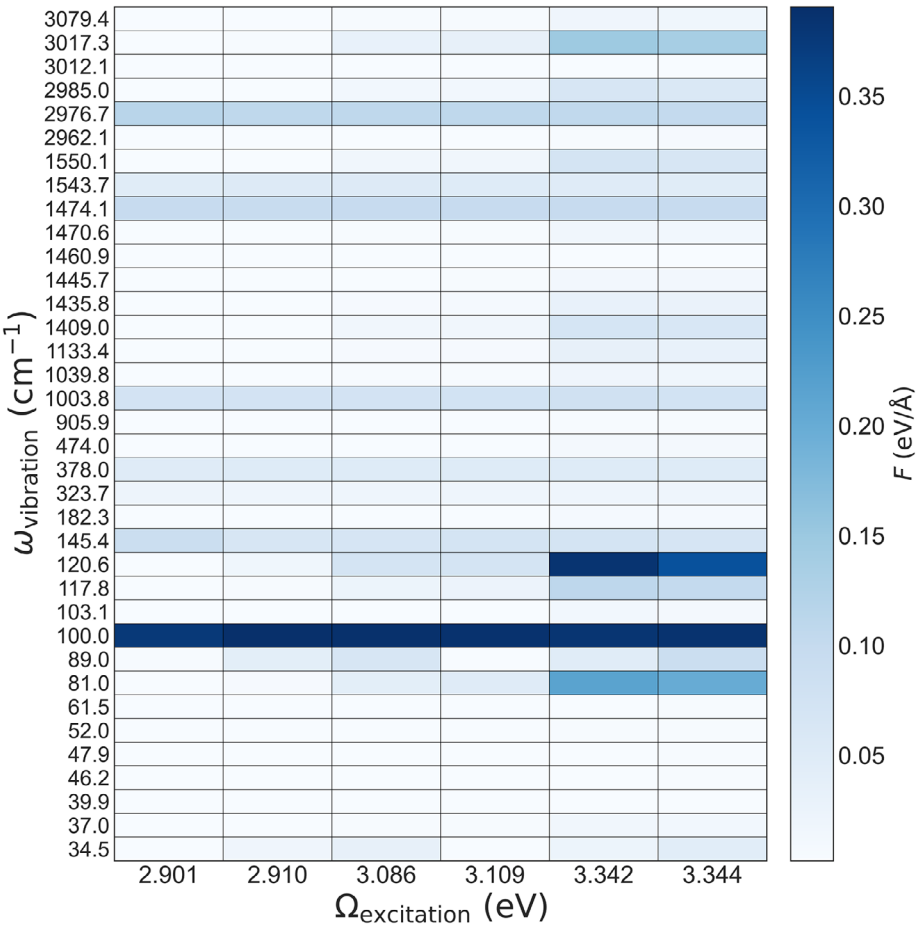

FIGURE 6 | Exciton-phonon coupling coefficients for lowest six excitons. The strongest exciton couples with a phonon of frequency 100 cm^{-1}, in accordance with the phonon frequency extracted from temperature-dependent FWHM of PL spectra in Figure 7.

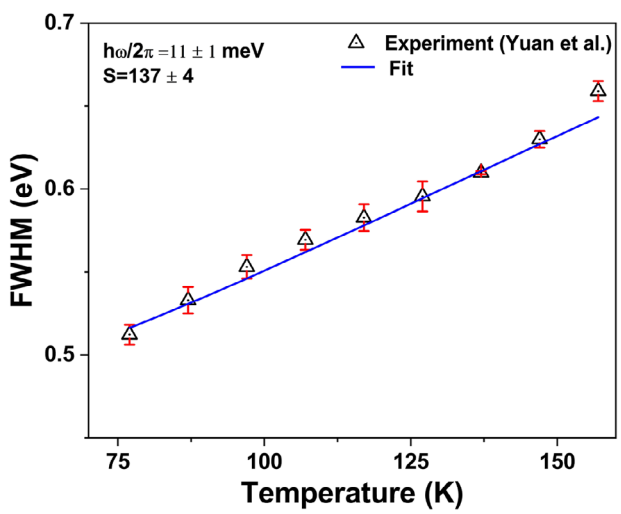

FIGURE 7 | The fitting results of PL full width at half maximum (FWHM) as a function of temperature, using PL from 77 to 300 K in steps of 10 K (extracted from Yuan et al. [5]) fit to a Gaussian function. The red error bars are due to standard error from the Gaussian fit.

optical absorption are polarization-dependent, a photodetector made from aligned OMHH crystals or films could serve as a built-in polarimeter, distinguishing light polarization without external filters. This could find use in polarization-resolved imaging or communication systems. Additionally, the broadband white-light emission from self-trapped excitons suggests the material could act as a single-component phosphor or active layer in white-light LEDs. Instead of using a mixture of different emitters to produce white light, a LED based on this material could emit across the visible spectrum inherently. This might simplify device architecture and improve color stability over time, as the emission comes from a single phase. Moreover, the fact that emission polarization is uniform regardless of excitation polarization means such an LED would emit polarized light, which could be advantageous in certain display or lighting applications requiring polarized output.

Beyond illumination and detection, low-dimensional hybrid perovskites like OMHH could be explored as sensors. The strong exciton–phonon coupling implies that the emission properties (peak energy, intensity, or bandwidth) are sensitive to lattice perturbations. This could be leveraged for sensing environmental factors such as temperature (thermally induced shifts in PL), pressure or strain (which would alter the lattice and thus the STE emission) [59], or chemical vapors that might intercalate between the chains and influence the lattice. A low-dimensional sensor device could thus be envisioned, where changes in the broadband emission signal indicate the presence of certain stimuli.

Even with state-of-the-art ultrafast diffraction, Å-level transient distortions in hybrid halides are difficult to resolve unambiguously. Our GW–BSE force framework complements this by providing a mode-resolved structural relaxation pathway in the excited state – i.e., explicit atomistic displacement vectors and resolution into the dominant phonons that drive self-trapping. Because light absorption and relaxation to the excited-state minimum occur on femto- to picosecond timescales, these theory-derived distortions offer concrete targets for time-resolved UED/tr-XRD and TR-XAFS (bond-selective) measurements, enabling direct validation of bond-length/angle changes during the early relaxation window. In this way, the theory supplies quantitative benchmarks (which bonds move, by how much, and via which vibrational modes), while ultrafast experiments can test those observables in real time, together establishing a rigorous, experimentally anchored picture of excited-state structural evolution.

Translating the anisotropic optical and transport response of OMHHs into practical devices also requires quantitative assessment of operational stability and scalable control of macroscopic orientation. Perovskites have already been explored for linearly polarization-sensitive photodetectors using (i) nominally 3D perovskites shaped into anisotropic nanostructures (for example, wires, ribbons, gratings, or platelets/rods) and (ii) intrinsically anisotropic low-dimensional (especially 2D) perovskites; in contrast, reports leveraging intrinsically 1D hybrid perovskites for polarization-sensitive photodetection remain limited [60]. Beyond detection, anisotropic perovskite nanostructures have also enabled directly linearly polarized LEDs (for example, nanoplatelet superlattices) [61], and more broadly, solution-processable crystals with large optical anisotropy have been demonstrated for efficient polarization manipulation [62]. For $DMEDAPbBr_4$, prior work indicates that free and self-trapped excitons remain active at room temperature and that the broadband emission persists under continuous excitation in air, with only a gradual decrease in photoluminescence intensity under high-power Hg-lamp illumination [5]. Nevertheless, device-relevant stability metrics should be established under controlled irradiance, temperature, oxygen, and humidity, and under electrical bias where applicable, together with encapsulation and barrier-layer approaches that are commonly used to mitigate moisture- and oxygen-driven degradation pathways in hybrid halide materials [63–65]. We also clarify that the well-known instability of Sn-based halide perovskites is strongly influenced by Sn(II) oxidation in the presence of oxygen [66]; while the present compound is Pb-based, environmental robustness against moisture and photoinduced defect chemistry remains an important engineering constraint [65]. Finally, device concepts based on anisotropy require macroscopic alignment of the chain axis, so scalable directed-growth or alignment routes (for example, solution shearing, shearing-assisted ordering, or template-directed patterning demonstrated in related perovskite systems) will likely be necessary to produce large-area, orientation-controlled films or aligned microcrystal arrays [67–69].

5 | Conclusion

In summary, our results provide valuable insights into the crystal structure, Raman spectroscopy, electrical conductivity, and excited-state dynamics of OMHH, a pseudo-one-dimensional material with unique properties. Our investigation into Raman spectroscopy emphasizes the importance of polarized measurements to understand the anisotropic nature of this material. The electrical conductivity analysis reveals strong anisotropy, with conductivity predominantly occurring along the Pb–Br chain direction. This guides how to properly apply the voltage bias for device applications, and anisotropic conduction could also potentially be useful in direct polarization detection devices. We also applied a new methodology to understand the excited-state dynamics and exciton-phonon coupling, via GW/BSE excited-state forces and a fit of the temperature-dependent PL. We found significant Huang-Rhys factor of 137 ± 4, indicating strong electron-phonon coupling. Our simulated phonon frequency corresponding to coupling agrees well with experiments. Further exploration of the dynamics of the structure due to excited-state forces in a larger supercell will provide insights into exciton self-trapping structures, contributing to understanding of the mechanisms for broadband emission and uniform polarization in emission, regardless of the polarization direction in absorption [18]. Future time-resolved structural and spectroscopic measurements, for example ultrafast X-ray diffraction and transient absorption, could directly test the predicted excited-state Pb–Br octahedral expansion and contraction and further strengthen the proposed mechanism.

Acknowledgements

This work was supported by the Air Force Office of Scientific Research under award number FA9550-19-1-0236, the National Science Foundation under Grant Nos. DMR-2144317 and DMR-2204466, and the Laboratory Directed Research and Development program of Los Alamos National Laboratory under award number 20230014DR. This work was performed in part at the Center for Integrated Nanotechnologies, an Office of Science User Facility operated for the U.S. Department of Energy Office of Science. Los Alamos National Laboratory is managed by Triad National Security, LLC for the U.S. Department of Energy's NNSA, under contract number 89233218CNA000001. This work used computational resources from the Multi-Environment Computer for Exploration and Discovery (MERCED) cluster at UC Merced, funded by National Science Foundation Grant No. ACI-1429783, and the National Energy Research Scientific Computing Center (NERSC), a U.S. Department of Energy Office of Science User Facility operated under Contract No. DE-AC02-05CH11231.

Conflicts of Interest

The authors declare no conflicts of interest.

Data Availability Statement

The data that support the findings of this study are available from the corresponding author upon reasonable request.

References

1. D. T. Gangadharan and D. Ma, "Searching for Stability at Lower Dimensions: Current Trends and Future Prospects of Layered Perovskite Solar Cells," *Energy & Environmental Science* 12 (2019): 2860–2889.

2. H. Lin, C. Zhou, Y. Tian, T. Siegrist, and B. Ma, "Low-Dimensional Organometal Halide Perovskites," *ACS Energy Letters* 3 (2018): 54–62.

3. C. Zhou, L.-J. Xu, S. Lee, H. Lin, and B. Ma, "Recent Advances in Luminescent Zero-Dimensional Organic Metal Halide Hybrids," *Advanced Optical Materials* 9 (2021): 2001766.

4. Y. Yang, F. Gao, S. Gao, and S.-H. Wei, "Origin of the Stability of Two-Dimensional Perovskites: A First-Principles Study," *Journal of Materials Chemistry A* 6 (2018): 14949–14955.

5. Z. Yuan, C. Zhou, Y. Tian, et al., "One-Dimensional Organic Lead Halide Perovskites with Efficient Bluish White-Light Emission," *Nature Communications* 8 (2017): 14051.

6. G. Wu, C. Zhou, W. Ming, et al., "A One-Dimensional Organic Lead Chloride Hybrid with Excitation-Dependent Broadband Emissions," *ACS Energy Letters* 3 (2018): 1443–1449.

7. S. Yang, Y. Wang, P. Liu, Y.-B. Cheng, H. J. Zhao, and H. G. Ya, "Functionalization of Perovskite Thin Films with Moisture-Tolerant Molecules," *Nature Energy* 1 (2016): 15016.

8. L. N. Quan, M. Yuan, R. Comin, et al., "Ligand-Stabilized Reduced-Dimensionality Perovskites," *Journal of the American Chemical Society* 138 (2016): 2649–2655.

9. H. Tsai, W. Nie, J.-C. Blancon, et al., "High-Efficiency Two-Dimensional Ruddlesden–Popper Perovskite Solar Cells," *Nature* 536 (2016): 312–316.

10. C. Ma, D. Shen, B. Huang, et al., "High-Performance Low-Dimensional Perovskite Solar Cells Based on a One-Dimensional Lead Iodide Perovskite," *Journal of Materials Chemistry A* 7 (2019): 8811.

11. J. Wu, Q.-F. Huang, Y.-F. Fu, et al., "Phase Engineering for Achieving Full-Color Tunable Emission from Blue to Red and Multi-Level Information Security in Isomeric Hybrid Copper Halides," *Angewandte Chemie International Edition* 64 (2025): e202506748.

12. J. Wu, Y. Guo, J.-L. Qi, et al., "Multi-Stimuli Responsive Luminescence and Domino Phase Transition of Hybrid Copper Halides with Nonlinear Optical Switching Behavior," *Angewandte Chemie International Edition* 62 (2023): e202301937.

13. R.-N. Li, Z.-C. Wu, W.-D. Yao, et al., "Hybrid Zinc-Based Halides with Giant Optical Anisotropy via Protonation-Engineered π-Conjugated Organic Group," *Advanced Functional Materials* 36 (2025): e25860.

14. E. R. Dohner, E. T. Hoke, and H. I. Karunadasa, "Self-Assembly of Broadband White-Light Emitters," *Journal of the American Chemical Society* 136 (2014): 1718–1721.

15. M. Georgiev, L. Mihailov, and J. Singh, "Self-Assembly of Broadband White-Light Emitters," *Pure and Applied Chemistry* 67 (1995): 447–456.

16. R. T. Williams and K. S. Song, "The Self-Trapped Exciton," *Journal of Physics and Chemistry of Solids* 51 (1990): 679–716.

17. H. Tanino, W. W. Rühle, and K. Takahashi, "Time-Resolved Photoluminescence Study of Excitonic Relaxation in One-Dimensional Systems," *Physical Review B* 38 (1988): 12716.

18. L. M. McClintock, L. Yuan, Z. Song, et al., "Surface Effects on Anisotropic Photoluminescence in One-Dimensional Organic Metal Halide Hybrids," *Small Structures* 4 (2023): 2200378.

19. X. Cheng, J. Ma, Y. Zhou, et al., "Optical Anisotropy of One-Dimensional Perovskite $c_4n_2h_{14}pbi_4$ Crystals," *Journal of Physics: Photonics* 2 (2020): 014008.

20. K. S. Song and R. T. Williams, *Self-Trapped Excitons* (Springer, 1996).

21. X. Jiang, Z. Xu, Y. Zheng, J. Zeng, K.-Q. Chen, and Y. Feng, "A First-Principles Study of Exciton Self-Trapping and Electric Polarization in One-Dimensional Organic Lead Halide Perovskites," *Physical Chemistry Chemical Physics* 24 (2022): 17323–17328.

22. R. R. Del Grande and D. A. Strubbe, "Revisiting Ab-Initio Excited-State Forces from Many-Body Green's Function Formalism: Approximations and Benchmark," arXiv:2502.05144 (2025).

23. J. Deslippe, G. Samsonidze, D. A. Strubbe, M. Jain, M. L. Cohen, and S. G. Louie, "BerkeleyGW: A Massively Parallel Computer Package for the Calculation of the Quasiparticle and Optical Properties of Materials and Nanostructures," *Computer Physics Communications* 183 (2012): 1269–1289.

24. D. A. Strubbe, "Optical and Transport Properties of Organic Molecules: Methods and Applications," Ph.D. dissertation, University of California, Berkeley, 2012.

25. S. Baroni, S. de Gironcoli, A. Dal Corso, and P. Giannozzi, "Phonons and Related Crystal Properties from Density-Functional Perturbation Theory," *Reviews of Modern Physics* 73 (2001): 515–562.

26. P. Giannozzi, S. Baroni, N. Bonini, et al., "QUANTUM ESPRESSO: A Modular and Open-Source Software Project for Quantum Simulations of Materials," *Journal of Physics: Condensed Matter* 21 (2009): 395502.

27. P. Giannozzi, O. Andreussi, T. Brumme, et al., "Advanced Capabilities for Materials Modelling with Quantum ESPRESSO," *Journal of Physics: Condensed Matter* 29 (2017): 465901.

28. J. P. Perdew, K. Burke, and M. Ernzerhof, "Generalized Gradient Approximation Made Simple," *Physical Review Letters* 77 (1996): 3865–3868.

29. M. Lazzeri and F. Mauri, "First-Principles Calculation of Vibrational Raman Spectra in Large Systems: Signature of Small Rings in Crystalline SiO_2," *Physical Review Letters* 90 (2003): 036401.

30. J. P. Perdew and Y. Wang, "Accurate and Simple Analytic Representation of the Electron–Gas Correlation Energy," *Physical Review B* 45 (1992): 13244.

31. D. R. Hamann, "Optimized Norm-Conserving Vanderbilt Pseudopotentials," *Physical Review B* 88 (2013): 085117.

32. M. van Setten, M. Giantomassi, E. Bousquet, et al., "The PseudoDojo: Training and Grading an 85-Element Optimized Norm-Conserving Pseudopotential Table," *Computer Physics Communications* 226 (2018): 39–54.

33. G. K. Madsen, J. Carrete, and M. J. Verstraete, "BoltzTraP2, a Program for Interpolating Band Structures and Calculating Semi-Classical Transport Coefficients," *Computer Physics Communications* 231 (2018): 140–145.

34. S. A. Solin and A. K. Ramdas, "Raman Spectrum of Diamond," *Physical Review B*, 1 (1970): 1687–1698.

35. K. Talit and D. A. Strubbe, "Stress Effects on Vibrational Spectra of a Cubic Hybrid Perovskite: A Probe of Local Strain," *Journal of Physical Chemistry C* 124 (2020): 27287–27299.

36. S. Lee, R. Karkee, A. Ben-Akacha, et al., "Bulk Assembly of Organic Metal Halide Nanoribbons," *Chemical Communications* 59 (2023): 3711–3714.

37. M. M. Masud, J. Viera, A. Ben-Akacha, B. Ma, and D. A. Strubbe, "Computational and Experimental Investigation of Chiral and Achiral Two-Dimensional Organic Lead Bromide Perovskites: Octahedral Distortions and Electronic and Optical Properties," *ChemPhysChem* 26 (2025): 202500423.

38. D. A. Strubbe, E. C. Johlin, T. R. Kirkpatrick, T. Buonassisi, and J. C. Grossman, "Stress Effects on the Raman Spectrum of an Amorphous Material: Theory and Experiment on *a*-Si:H," *Physical Review B* 92 (2015): 241202.

39. L. Bastonero and N. Marzari, "Automated All-Functionals Infrared and Raman Spectra," *npj Computational Materials* 10 (2024): 55.

40. A. M. Leguy, A. R. Goñi, J. M. Frost, et al., "Dynamic Disorder, Phonon Lifetimes, and the Assignment of Modes to the Vibrational Spectra of Methylammonium Lead Halide Perovskites," *Physical Chemistry Chemical Physics* 18 (2016): 27051–27066.

41. P. Ghaemi, R. S. K. Mong, and J. E. Moore, "In-Plane Transport and Enhanced Thermoelectric Performance in Thin Films of the Topological Insulators Bi_2Te_3 and Bi_2Se_3," *Physical Review Letters* 105 (2010): 166603.

42. E. Kioupakis, M. L. Tiago, and S. G. Louie, "Quasiparticle Electronic Structure of Bismuth Telluride in the *GW* Approximation," *Physical Review B* 82 (2010): 245203.

43. J. B. Park, W. Wu, J. Y. Wu, et al., "Enabling Oxidation Protection and Carrier-Type Switching for Bismuth Telluride Nanoribbons via In Situ Organic Molecule Coating," *Nano Letters* 23 (2023): 11395–11401.

44. A. M. Ummah, Y.-C. Su, Y.-H. Peng, Y.-X. Xu, and C.-H. Ho, "Exploration of Quasi-Direct Band Edge in a Multilayer Ferroelectric Semiconductor for Applications in van der Waals Stacked Heterojunction Solar Cell and Photocatalytic Devices," *Advanced Science* 13 (2026): 202514717.

45. J. Guo, W. Xu, J. Cao, and X. Wei, "Novel Three-Dimensional TiO_2 Structure with a Unique Quasi-Direct Band Gap for Photocatalysts," *Physical Chemistry Chemical Physics* 25 (2023): 13623–13629.

46. C. He, C. Zhang, J. Li, et al., "Direct and Quasi-Direct Band Gap Silicon Allotropes with Remarkable Stability," *Physical Chemistry Chemical Physics* 18 (2016): 9682–9686.

47. W. Zhang, C. Chai, Q. Fan, Y. Song, and Y. Yang, "Direct and Quasi-Direct Band Gap Silicon Allotropes with Low Energy and Strong Absorption in the Visible for Photovoltaic Applications," *Results in Physics* 18 (2020): 103271.

48. Q. Ding, Y. Zhu, L. Xiang, et al., "Terahertz Direct Polarization Detector Based on Integrated Antenna-Coupled AlGaN/GaN High-Electron-Mobility Transistors," *Optics Express* 30 (2022): 42 956–42 966.

49. A. Li, C. Hu, B. He, et al., "Demonstration of Valley Anisotropy Utilized to Enhance the Thermoelectric Power Factor," *Nature Communications* 12 (2021): 5408.

50. R. Improta, F. Santoro, and L. Blancafort, "Quantum Mechanical Studies on the Photophysics and the Photochemistry of Nucleic Acids and Nucleobases," *Chemical Reviews* 116 (2016): 3540–3593.

51. S. Ismail-Beigi and S. G. Louie, "Self-Trapped Excitons in Silicon Dioxide: Mechanism and Properties," *Physical Review Letters* 95 (2005): 156401.

52. D. Wang, M. Wright, N. K. Elumalai, and A. Uddin, "Stability of Perovskite Solar Cells," *Solar Energy Materials and Solar Cells* 147 (2016): 255–275.

53. M. Jørgensen, K. Norrman, S. A. Gevorgyan, T. Tromholt, B. Andreasen, and F. C. Krebs, "Stability of Polymer Solar Cells," *Advanced Materials* 24 (2012): 580–612.

54. J. Luo, X. Wang, S. Li, et al., "Efficient and Stable Emission of Warm-White Light from Lead-Free Halide Double Perovskites," *Nature* 563 (2018): 541–545.

55. W. Stadler, D. M. Hofmann, H. C. Alt, et al., "Optical Investigations of Defects in $Cd_{1-x}Zn_xTe$," *Physical Review B* 51 (1995): 10619–10630.

56. T. H. Keil, "Shapes of Impurity Absorption Bands in Solids," *Physical Review* 140 (1965): A601–A617.

57. M. Lax, "The Franck–Condon Principle and Its Application to Crystals," *Journal of Chemical Physics* 20 (1952): 1752–1760.

58. Y. Zhang, "Applications of Huang–Rhys Theory in Semiconductor Optical Spectroscopy," *Journal of Semiconductors* 40 (2019): 091102.

59. Y. Wang, S. Guo, H. Luo, et al., "Reaching 90% Photoluminescence Quantum Yield in One-Dimensional Metal Halide $c_4n_2h_{14}pbbr_4$ by Pressure-Suppressed Nonradiative Loss," *Journal of the American Chemical Society* 142 (2020): 16001–16006.

60. J. Sun and L. Ding, "Linearly Polarization-Sensitive Perovskite Photodetectors," *Nano-Micro Letters* 15 (2023): 90.

61. J. Ye, A. Ren, L. Dai, et al., "Direct Linearly Polarized Electroluminescence from Perovskite Nanoplatelet Superlattices," *Nature Photonics* 18 (2024): 586–594.

62. Y. Zhou, Z. Guo, H. Gu, et al., "A Solution-Processable Natural Crystal with Giant Optical Anisotropy for Efficient Manipulation of Light Polarization," *Nature Photonics* 18 (2024): 922–927.

63. Q. Ma, S. Huang, X. Wen, M. A. Green, and A. Ho-Baillie, "Encapsulation Strategies for Stable Perovskite Solar Cells," *Energy & Environmental Science* 15 (2022): 13–55.

64. J. Li, R. Xia, W. Qi, et al., "Encapsulation of Perovskite Solar Cells for Enhanced Stability: Structures, Materials and Characterization," *Journal of Power Sources* 485 (2020): 229313.

65. N. Kore, S. Dehariya, V. Kumar, A. Singh, and P. Sahay, "Moisture: Impact on Stability and Strategies to Improve Stability of Hybrid Perovskites," *Materials Advances* 5 (2024): 695–717.

66. J. Pascual, M. A. Flatken, R. Felix, et al., "Origin of Sn(II) Oxidation in Tin Halide Perovskites," *Materials Advances* 1 (2020): 1066–1076.

67. C. Li, S. Tscheuschner, F. Paulus, et al., "Solution Coating of Superior Large-Area Flexible Perovskite Thin Films with Controlled Crystal Packing," *Advanced Optical Materials* 5 (2017): 1700102.

68. Z. Liu, B. Chen, Y. Yang, et al., "Simultaneous Mechanical and Chemical Synthesis of Long-Range-Ordered Perovskites," *Nature Synthesis* 4 (2025): 196–208.

69. L. Zhang, J. Li, Z. He, H. Chen, and Y. Zou, "Oriented Surface Arrays on Perovskite Single-Crystal Thin Films for Enhanced Polarization Sensing," *Optical Materials* 157, (2024): 116251.

Supporting Information

Additional supporting information can be found online in the Supporting Information section.

Supporting Information: admt70981-sup-0001-SuppMat.pdf.